Perfusion quantification by model-free arterial spin labeling using nonlinear stochastic regularization deconvolution.

Ahlgren, André; Wirestam, Ronnie; Petersen, Esben Thade; Ståhlberg, Freddy; Knutsson, Linda

Published in:
Magnetic Resonance in Medicine

DOI:
10.1002/mrm.24587

2013

Perfusion Quantification by Model-Free Arterial Spin Labelling Using Nonlinear Stochastic Regularization Deconvolution

André Ahlgren (1), Ronnie Wirestam (1), Esben Thade Petersen (2), Freddy Ståhlberg (1,3), Linda Knutsson (1)

(1) Department of Medical Radiation Physics, Lund University, Lund, Sweden
(2) Department of Radiology, University Medical Center Utrecht, Utrecht, The Netherlands
(3) Department of Diagnostic Radiology, Lund University, Lund, Sweden

Corresponding Author:
André Ahlgren
Department of Medical Radiation Physics
Barngatan 2:1
Lund University Hospital
SE 221 85 LUND
Sweden
Fax: +46 46 17 85 40
Andre.Ahlgren@med.lu.se

Word count: 4810
Running title: Deconvolution Methods in Model-Free ASL
Keywords: arterial spin labelling; deconvolution; cerebral blood flow

Abstract

Purpose: Quantification of cerebral blood flow (CBF) can be accomplished by model-free arterial spin labelling (ASL) using the QUASAR sequence. The required deconvolution is normally based on block-circulant singular value decomposition (cSVD/oSVD), an algorithm associated with non-physiological residue functions and potential effects of arterial dispersion. The aim of this work was to amend this by implementing nonlinear stochastic regularization (NSR) deconvolution, previously used to retrieve realistic residue functions in dynamic susceptibility contrast MRI.

Methods: To characterize the residue function in model-free ASL, and possibly to improve absolute CBF quantification, NSR was applied to deconvolution of QUASAR data. For comparison, SVD-based deconvolution was also employed. Residue function characteristics and CBF values from ten volunteers were obtained. Simulations were performed to support the in vivo results.

Results: NSR was able to resolve realistic residue functions in contrast to the SVD-based methods. Mean CBF estimates in grey matter were 36.6±2.6, 28.6±3.3, 40.9±3.6 and 42.9±3.9 ml/100g/min for cSVD, oSVD, NSR and NSR with correction for arterial dispersion, respectively. In simulations, the NSR-based perfusion estimates showed better accuracy than the SVD-based approaches.

Conclusion: Perfusion quantification by model-free ASL is evidently dependent on the selected deconvolution method, and NSR is a feasible alternative to SVD-based methods.

Introduction

Magnetic resonance imaging (MRI) is widely used for measurements of perfusion (1-4), and assessment of cerebral blood flow (CBF) is very important in diagnosis and characterization of cerebrovascular disorders, such as ischaemic stroke, as well as in tumor grading and monitoring of tumor therapy (5-7). Also, perfusion MRI has shown increasing potential in the diagnosis and prediction of neurodegenerative diseases, for example, Alzheimer's and Parkinson's disease (8,9). Whereas most standard methods for perfusion mapping employ radioactive tracers or exogenous contrast agents, arterial spin labelling (ASL) is a non-invasive alternative in which arterial blood water is used as an endogenous tracer (3,4). In general, ASL measures the change in the longitudinal magnetization obtained by labelling (i.e., inverting or saturating) spins in arterial blood upstream of the imaging region. Thus, after subtraction from a control image, obtained without labelling, only the longitudinal magnetization difference (ΔM), which reflects regional perfusion, remains.

Petersen et al. (10) applied the general kinetic model (11) by developing an ASL sequence capable of sampling both ΔM as a function of time and local arterial input functions (AIFs), enabling the perfusion-scaled residue function, and subsequently CBF, to be estimated by means of model-free deconvolution. This approach, referred to as model-free ASL, avoids parametric modelling of the system and also makes the perfusion quantification less dependent on arterial transit time. However, application of model-free deconvolution to dynamic susceptibility contrast MRI (DSC-MRI) has previously indicated that the CBF quantification may be dependent on the specific deconvolution algorithm used (2,12,13).

Petersen et al. (10) employed block-circulant singular value decomposition (cSVD) deconvolution (13). The cSVD method generally produces robust CBF maps, but the choice of thresholding to truncate high-frequency components, and thereby suppress spurious oscillations of the solution, tends to affect the shape of the solution and bias the CBF values (14). A common approach for improvement is to employ an adaptive threshold through an oscillation measure (oSVD) (13). Both cSVD and oSVD frequently return non-monotonically decreasing solutions as well as negative values, and this is in direct violation of the definition of the residue function, which should be a smooth, nonnegative, decreasing function of time. Furthermore, CBF values obtained by deconvolution are prone to underestimation due to arterial dispersion, since it is difficult to measure AIFs close to the local capillary system of interest (15). This raises the question of whether more suitable deconvolution methods are available for model-free ASL.

While cSVD or oSVD might be sufficient in many cases, a wide variety of alternative model-free deconvolution methods have been proposed for application to DSC-MRI data. Many methods are based on improving the residue function characteristics by incorporating *a priori* information of the shape, or accounting for arterial delay and/or dispersion (16-18). Zanderigo et al. (19) proposed a nonlinear Bayesian approach called nonlinear stochastic regularization (NSR). The smoothness and nonnegativity of the solution is included as *a priori* information and the method also attempts to correct for arterial dispersion.

To the best of our knowledge, however, only SVD-based deconvolution has previously been applied to model-free ASL. The SVD-based algorithms tend to produce unrealistic residue functions, which questions the reliability of the corresponding perfusion estimates, and alternative deconvolution methods could help improving perfusion estimates obtained by model-free ASL. In this work, we therefore demonstrate the implementation of NSR in the

model-free ASL framework using the QUASAR sequence, and compare residue function characteristics and CBF values to those obtained by SVD-based methods.

Theory

Perfusion quantification

Perfusion quantification in model-free ASL (10) is based on the general kinetic model, proposed by Buxton et al. (11), and employs deconvolution of the time-resolved perfusion signal, $\Delta M(t)$, and the corresponding AIF:

$$\Delta M(t) = 2 \cdot M_{0,a} \cdot f \cdot [c(t) \otimes R(t)] \quad [1]$$

where "⊗" denotes convolution, $M_{0,a}$ is the magnetization of fully relaxed arterial blood, f is tissue perfusion, $c(t)$ is the fractional AIF and $R(t)$ is residue function, i.e., the fraction of label that remains at time t (taking effects of wash-out and relaxation into account) after an instantaneous input. The absolute AIF is defined as $C_{AIF}(t) = 2 \cdot M_{0,a} \cdot c(t)$, so that deconvolution of $\Delta M(t)$ with $C_{AIF}(t)$ yields the perfusion-scaled residue function $f \cdot R(t)$ and f can, ideally, be obtained from the zero time point of the solution. It is common, however, to calculate f as the maximum value of $f \cdot R(t)$ since most deconvolution methods produce solutions with an initial increase, often associated with arterial delay and/or dispersion.

In model-free ASL, a pulse sequence called QUASAR (quantitative STAR labeling of arterial regions) (10) is applied, exploiting a pulsed ASL labeling scheme and readout by multiple low flip angle acquisition, consequently measuring a saturation recovery. The scan is performed both with and without crusher (spoiler) gradients to obtain vascular signals that constitute a good estimate of $c(t)$. $C_{AIF}(t)$ is calculated by scaling $c(t)$ with $M_{0,a}$ and correcting for labeling efficiency and saturation due to the multiple read-out pulses. The theory of model-free ASL is explained in detail by Petersen et al. (10,20,21).

Nonlinear stochastic regularization

The NSR method, as proposed in (19), employs Bayesian statistics to estimate the solution:

$$f \cdot R(t) = \mathrm{e}^{k+\theta_2 \cdot \beta(t)} \otimes d(t) \quad [2]$$

where k and θ_2 are unknown scalars, $\beta(t)$ is a Wiener process, representing the stepwise integral of white Gaussian noise, and

$$d(t) = \frac{1}{\theta_1} \mathrm{e}^{-t/\theta_1} \quad [3]$$

is a dispersion kernel with the unknown scalar θ_1 corresponding to the amount of arterial dispersion (15). The inclusion of the dispersion kernel allows the undispersed solution to be reproduced, thereby correcting the CBF estimates for arterial dispersion. NSR reproduces the solution on an arbitrary temporal resolution (often higher than the sampling frequency) set by the user.

The NSR optimization can be formulated in matrix form where $\mathbf{y}$ is the measured tissue signal, $\mathbf{G}$ is the convolution with $C_a(t)$, $\mathbf{\Sigma_v}$ is the square diagonal covariance matrix of measurement noise with diagonal elements equal to the variance of the tissue signal at

different sample times, multiplied by an additional unknown scalar θ_3, and $\mathbf{R_1}$ is the function to be estimated. The unknown scalars θ_1, θ_2, θ_3, k and γ (the regularization parameter controlling the smoothness of the solution) are determined by marginal likelihood estimation and the maximum *a posteriori* estimate of $\mathbf{R_1}$ is then given by:

$$\widehat{\mathbf{R}}_{\mathbf{1}} = \arg\min_{\mathbf{R_1}} \left[(\mathbf{y} - \mathbf{G}[\mathbf{d} \otimes \mathrm{e}^{\mathbf{R_1}}])^T \, \boldsymbol{\Sigma}_v^{-1} \, (\mathbf{y} - \mathbf{G}[\mathbf{d} \otimes \mathrm{e}^{\mathbf{R_1}}]) + \gamma^{-2} \int \left(\dot{\mathbf{R}}_{\mathbf{1}}\right)^2 dt \right] \qquad [4]$$

where $\dot{\mathbf{R}}_{\mathbf{1}}$ is the time derivative of $\mathbf{R_1}$. Since the undispersed solution and the dispersion kernel are separated in the optimization process, both the dispersed and the dispersion corrected residue functions are obtained simultaneously. It is important to emphasize that NSR is not a parametric model in the deterministic sense even if, in a way, $f \cdot R(t)$ is modelled. The solution is specified over an infinite dimensional function space, i.e., it does not describe a certain shape, and NSR can thus be viewed as a tradeoff between model-free methods with no *a priori* information and parametric methods which fully describe the shape of the solution. The theory of NSR is explained in detail by Zanderigo et al. (19,22).

To apply NSR to time-resolved ASL data, some modifications were required. Firstly, in our implementation, the measurement noise (i.e., the diagonal elements of the covariance matrix) was modelled as $[\theta_3 \cdot SD_{\Delta M}(t_i)]^2$, where $SD_{\Delta M}(t_i)$ is the sample standard deviation of ΔM at time t_i. Secondly, NSR is not delay insensitive (23) which introduces bias in the solution for model-free ASL data if the macrovascular transit time is long. However, the original QUASAR methodology includes an automatic temporal shift so that the rising edge of the AIF coincided with the rising edge of the tissue signal. A similar automatic shift was used in this work, to ensure optimal and equivalent inputs to all deconvolution methods.

Methods

Simulations

Perfusion estimation using the different deconvolution methods was simulated using the standard model for pulsed ASL (11), although with the modified Hrabe-Lewis model for the AIF. The signal-to-noise-ratio (SNR) was defined as $\Delta M(t_{max})/\mathrm{SD}_{\Delta \mathrm{M}}(t_{max})$, where t_{max} is the discrete time point at which $\Delta M(t)$ is maximal. The noise level was estimated from in vivo data, yielding a SNR of approximately 1-3 in GM voxels (although many voxels showed considerably lower SNR levels). The simulations was performed with perfusion values of 1–100 ml/100g/min, SNR levels of 0.3, 1 and 3 (for a perfusion value of 50 ml/100g/min), and with 1000 noise realizations for each combination. Since NSR exploits the measured standard deviation of $\Delta M(t)$, each simulation iteration used 25 repetitions. All experimental parameters and deconvolution priors were identical to the ones used for the in vivo data (see MRI experiments section). Tissue relaxation, arterial blood relaxation, brain-blood partition coefficient and arterial transit time were set to 1.4 s, 1.65 s, 0.9 ml/g and 0.25 s respectively. To evaluate the residue function characteristics, the root-mean-square error (RMSE) of the resolved residue functions was calculated for a variety of perfusion values and SNRs. The delay sensitivity of the deconvolution methods was assessed by using an identical simulation setup, with varying delays between the AIF and tissue curve. This simulation was performed both with and without the automatic temporal shift, using delay times of -0.5–1 s, a perfusion value of 50 ml/100g/min and SNR=2.

MRI experiments

In this study, data from ten volunteers (6 males, 4 females, age 21-65 years), participating in a previous multi-center QUASAR study (20), were used. The study was approved by the local ethics committee, and all volunteers gave written informed consent. The experiments were performed on a 3T MRI unit (Philips Achieva, Philips Healthcare, Best, The Netherlands) using an 8 channel SENSE receiver head coil. In the QUASAR (20) imaging protocol, the following general parameters were used: 7 slices, 6 mm slice thickness, 2 mm slice gap, 64×64 matrix, 240×240 mm^2 FOV, 35°/11.7° flip angles, TR/TE/ΔTI/TI_1=4000/23/300/40 ms, 640 ms bolus length, 13 inversion times, 84 series (48 crushed, 24 non-crushed and 12 low flip angle - alternating label and control), 4 cm/s velocity encoding for the crushed pairs, 2.5 SENSE factor, 150 mm labelling thickness, at a total scan time of 5 min 52 s.

Post-processing

All post-processing software tools were executed on a PC using MATLAB 2010b (The MathWorks, Inc., Natick, MA, USA). An in-house developed software was used, based on the theory in Ref. (21), the QUASAR post-processing software source code (developed by ET Petersen), and available NSR code (19). The main purpose of the locally developed software was to take a QUASAR data set consisting of 7644 2D images, automatically produce $C_{AIF}(t)$ and $\Delta M(t)$ data for every brain voxel, and apply the deconvolution algorithms.

Single ΔM images with large deviations from the mean value were assumed artifactual and omitted in the averaging, and $\Delta M(t)$ was calculated by averaging the remaining images for every time point. Longitudinal relaxation time, T_{1t}, and equilibrium magnetization in tissue, $M_{0,t}$, were mapped by fitting the signal equation to the measured saturation recovery and correcting for the multiple read-out pulses. Voxel-wise fractional volumes of cerebrospinal fluid (CSF), grey matter (GM) and white matter (WM) were estimated by a segmentation method exploiting the inherent saturation recovery of the QUASAR sequence (24,25). The fractional volumes and $M_{0,t}$ were used to calculate a voxel-wise $M_{0,a}$, taking into account the true distribution volume (excluding CSF) and a spatially varying brain-blood partition coefficient (24).

Potential AIFs were identified as voxels with an estimated arterial blood volume higher than 1.2% (10). To avoid noisy AIFs, and to allow for high-resolution AIFs for the NSR deconvolution, the modified Hrabe-Lewis model (26) was fitted to each of the potential AIFs (discarding AIFs with large root-mean-square deviations). Each tissue voxel was paired with its closest AIF. The rising edges of the crushed and non-crushed time series were estimated by Canny edge detection (27) and the resulting transit times were used to correct for the saturation, due to the read-out pulses, of the labelled spins while travelling from the site of the measured AIF to the capillary system. The rising edge of the crushed signal was used together with the arterial transit time of the fitted AIF for an automatic temporal shift of $C_{AIF}(t)$ to avoid delay effects. A unique $C_{AIF}(t)$ was then produced for every voxel by a scaling based on the local $M_{0,a}$ and the temporal shift. For the AIF scaling it was also assumed that the longitudinal relaxation of arterial blood was 1.65 s (28), the bolus length was 640 ms, and the labelling efficiency was 0.95 (21).

The pairwise $C_{AIF}(t)$ and $\Delta M(t)$ curves were deconvolved using NSR, NSR with correction for dispersion (NSRcd), cSVD and oSVD. The NSR code (19) was modified as described in the theory section, using a virtual time grid increment of 25 ms and starting parameters θ_1=0.1, θ_2=1 and θ_3=0.2, based on empirical experience. The cSVD and oSVD

deconvolution algorithms were based on the methods described by Wu et al., with a threshold value P_{SVD}=0.2, and an oscillation index threshold of 0.095 (13).

Analysis

The mean CBF value in GM, CBF_{GM}, was evaluated by producing a GM mask based on the fractional volumes from the segmentation. Voxels with more than 80% grey matter were included in the mean value. To improve the comparison between methods, voxels showing a perfusion level below 1 ml/100g/min using any of the investigated methods, were omitted from the mean value across all methods (see Discussion). The mean CBF_{GM} estimates of the four methods were tested for significant differences by one-way analysis of variance (ANOVA) followed by multiple comparison with Tukey's range test, both with a significance level of 0.05. The effect of the dispersion correction in NSR was summarized by calculating the amount of GM voxels for which the dispersion correction had an effect (>1%) on the CBF value, and also by calculating the magnitude of those corrections.

To assess the spatial variability of perfusion maps and dispersion effects generated by the different methods, relaxation rate ($1/T_{1t}$) maps from QUASAR were nonlinearly coregistered (spatially normalized) to the MNI152 template brain (ICBM, NIH P-20 project) using SPM8 (29). The spatial transform was then applied to the parametric maps of interest for each subject, creating group mean parametric maps. In addition, absolute (ΔCBF) and relative ($rel\Delta CBF$) maps of the perfusion difference between NSRcd and oSVD were produced. The $rel\Delta CBF$ maps were calculated by scaling with CBF_{GM} (for each method and subject) with subsequent spatial normalization and subtraction of the group mean relative perfusion maps.

Results

Simulations

In Figure 1, results from simulations of the perfusion and residue function estimations are provided. The top row (Fig. 1 a-c) shows perfusion estimates for three different SNRs. As an example, for a true perfusion of 50 ml/100g/min and SNR=1, simulated perfusion values were 37.3±9, 23.4±10, 46.4±15 and 48.6±18 ml/100g/min (mean ± standard deviation) for cSVD, oSVD, NSR and NSRcd, respectively. The NSR methods showed generally higher standard deviations. Figure 1 d-i shows mean resolved residue functions for the different methods at five perfusion values, and the corresponding RMSEs of the residue functions are given in Figure 2. The results from the simulation of delay sensitivity are displayed in Figure 3 (dashed lines correspond to no delay correction). The top row (Fig. 3 a-b) shows estimated perfusion for all methods and estimated dispersion in NSR, respectively, as a function of delay. Figure 3 c-f exhibits the mean resolved residue functions for different delays.

Residue function characteristics

Figure 4 shows $f \cdot R(t)$ and the corresponding reconvolved tissue signals in a single GM voxel in one volunteer. This voxel is representative for GM and selected to reflect the general patterns of obtained CBF maps. The cSVD method consistently produced solutions with oscillations and negative values, whereas oSVD generally succeeded in regularizing the oscillations. On the other hand, NSR produced solutions with smooth shape and nonnegative values, and NSRcd also resulted in solutions with monotonic decrease, i.e., without the effect of dispersion.

Figure 5 displays density plots of normalized GM residue functions for the different deconvolution algorithms. The SVD-based methods showed almost exclusively non-monotonically decreasing solutions with negative values. The SVD-based solutions generally converged to zero and the spread was fairly limited (first and third quartiles were reasonably close to the median). The NSR method resulted in nonnegative values but showed fewer voxels that converged to zero, and NSRcd returned, in addition, almost exclusively monotonically decreasing solutions.

Cerebral blood flow

Examples of CBF maps from a single slice in subject 1 are shown in Figure 6. The result of the perfusion quantification is presented in Table 1 and Figure 7. The mean CBF_{GM} estimates (i.e., for all subjects) for the different methods were 36.6±2.6, 28.6±3.3, 40.9±3.6 and 42.9±3.9 ml/100g/min (mean ± standard deviation) for cSVD, oSVD, NSR and NSRcd, respectively. The corresponding mean coefficient of variation (COV) of CBF values in GM for each method was 41.0 %, 46.3%, 63.2% and 63.0%, respectively. The statistical analysis indicated that mean CBF_{GM} showed a significant dependence on deconvolution method ($p<0.05$), although results obtained by NSR and NSRcd were not significantly different.

Analysis of the dispersion correction showed that for 42% of the GM voxels, the dispersion correction had only a negligible effect (<1%) on the peak $f \cdot R(t)$ value. For the remaining GM voxels, the peak $f \cdot R(t)$ value was 9.4±2.0% (mean ± standard deviation) higher after dispersion correction, with 54% of these voxels showing a dispersion correction effect exceeding 5%.

Finally, it was observed that for very noisy voxels showing no apparent tissue signal at visual inspection, NSR generally resulted in a CBF value of 0 ml/100g/min, whereas SVD returned an unpredictable perfusion value due to overfitting.

Spatial variability

Figure 8 shows results from the spatial variability analysis in one centrally located slice. The left column (Fig. 8 a,d,g) serves as anatomical reference, Fig. 8 b-c displays absolute perfusion and Fig. 8 e-f shows ΔCBF and $rel\Delta CBF$. NSRcd returned generally higher values in areas where large arteries are expected, whereas oSVD displayed higher relative perfusion in areas with long arrival time. Figure 8 h shows the estimated dispersion (θ_1) and Fig. 8 i exhibits the time of the rising edge of the crushed signal (microvascular arrival time; τ_m). The estimated dispersion was higher in areas with long τ_m and high fractional WM (cf. Fig. 8 g).

Discussion

Simulations

The simulations showed that for low SNR (Fig. 1 a), all methods tended to underestimate perfusion (except for low perfusion values where cSVD resulted in overestimation). The SVD-based methods showed a linear relation between estimated and true CBF, although with a slope < 1, whereas the corresponding NSR-based relationships were nonlinear at low SNR. NSR showed good agreement between estimated and true perfusion for higher SNR (Fig. 1 b-c), and perfusion values obtained by NSR were generally less biased than SVD-based methods, given a reasonable SNR. Although the perfusion estimates obtained by NSRcd were satisfactory (Fig. 1), the RMSE was much higher compared with NSR (Fig. 2), and this is

clearly a result of the fact that residue functions produced by NSRcd did not converge to zero (cf. Fig. 1 i). This might imply that NSR produces the most reliable residue function shapes (although not monotonically decreasing), whereas NSRcd best estimates the perfusion. It should be noted that the starting value of θ_1 was set to 0.1 to reflect the settings used in the in vivo analysis, even though no dispersion effects were included in the simulations.

Results from the simulation of delay sensitivity suggested that the automatic temporal shift performed satisfactorily (Fig. 3). NSR deconvolution in general, and NSRcd in particular, tended to be very delay sensitive when no correction was applied, whereas cSVD and oSVD were, as expected, rather insensitive to delay (Fig. 3 a). It should be noted that Fig. 3 c-d only displays the first half of the solutions (which is why the wrap-around is not visual), and that our implementation of cSVD/oSVD seemed to be sensitive to negative delays. When no correction was used for positive delays, NSR optimization increased the delay parameter in order to better fit the measured tissue signal (Fig. 3 b).

Residue function characteristics

Every dataset results in thousands of residue functions which makes it difficult to display any general behavior. Figure 4, however, represents a very common outcome in GM voxels, and Fig. 5 indicate the general patterns of residue functions in GM. In general, cSVD displayed a tendency of overfitting to the measured data which resulted in spurious oscillations, while oSVD suppressed these oscillations, apparently at the cost of also suppressing peak values (i.e., the perfusion estimates). Furthermore, the SVD-based methods consistently violated the criteria of a residue function. The NSR methods, on the other hand, produced more realistic solutions, with characteristics such as more continuous (non-oscillating) behavior and nonnegative values. Also, NSRcd was capable of recreating undispersed residue functions with a monotonic decrease. This means that the perfusion estimate can be extracted from the zero time point of the solution. The initial increase of the residue functions returned by NSR (without correction for dispersion) and by the SVD methods (Fig. 5 a-c), indicate that dispersion may have a significant effect on the solution, and thus on the perfusion estimates, in model-free ASL. On the other hand, similar solutions were seen with simulations carried out without dispersion (Fig. 1).

Although NSR, in general, showed much more reasonable residue function characteristics than the SVD-based methods, there are presently some issues to be mentioned. The current NSR implementation lacks criteria concerning monotonically decreasing solutions, as well as to the zero limit when time approaches infinity. The former condition rarely causes any problem, but solutions that do not converge to zero were frequently observed (as also seen in the simulations; Fig. 1 h-i). This is explained by the fact that $\Delta M(t)$ has not reached baseline at the time of the last readout, and the residue function characteristics might benefit from expanding the model to include these criteria.

Cerebral blood flow

Perfusion maps produced by cSVD and oSVD were more homogeneous (i.e., showed lower degree of differentiation within and between different brain regions) than those produced by NSR and NSRcd (Fig. 6), confirmed by the overall higher COV for NSR/NSRcd than for cSVD/oSVD. The SVD-based methods are known to regularize the quantification (10), depending on threshold parameters, potentially to such an extent that obtained values are underestimated, and our result may thus indicate a spurious homogeneity. This agrees with

our simulations showing that higher perfusion values were more underestimated (Fig. 1 a-e), which would result in more homogenous values in a tissue volume with varying true perfusion levels.

The methods yielded significantly different perfusion estimates, with CBF_{GM} being approximately 50% higher with NSRcd compared to oSVD, which is most likely related to the regularization in oSVD. This agrees with previous (13,19) and our simulations (Fig. 1), showing that NSR more accurately estimates perfusion while SVD-based methods are prone to underestimation. Allowing a higher oscillation index in oSVD indeed would increase the perfusion values, although at the cost of less contrast in the perfusion maps. Perfusion estimates obtained by SVD-based methods are extremely dependent on selected thresholds, whereas NSR estimates the regularization parameter automatically in every voxel, not relying on any predefined thresholds.

The inter-individual spread in CBF_{GM} was reasonable, but the absolute mean values were somewhat lower than expected for healthy volunteers, with normal PET-based GM perfusion values being of the order of 50–60 ml/100g/min (30). Petersen et al. reported a QUASAR-based mean GM perfusion value of 47.4 ml/100g/min using a SVD-based approach (20), although with a post-processing and analysis procedure which differed slightly from the one used in the present study. The present results suggest that the low CBF_{GM} values obtained with model-free ASL may partially be due to the deconvolution method.

The obtained perfusion estimates are also likely to depend on the selected model for the AIF. A common approach is to model AIFs by a gamma-variate function, but lately, more sophisticated models have appeared. We chose to employ the modified Hrabe-Lewis model (i.e., a spatial reformulation of the Gaussian dissipation function) since it describes a boxcar-shaped bolus that is dispersed in a probabilistic manner, which implies that it is easier to justify from a physics and physiology perspective. Hence, the dispersion between the labelling site and the measured AIF was modelled slightly differently than the dispersion between the AIF site and the tissue voxel. Perfusion estimates obtained by NSR also depend on the temporal shift of the AIF. To minimize this influence, the shift should be selected so that the resulting signal curves reflect realistic input and response (output) from a time-invariant linear system. Our simulations (Fig. 3) confirmed that our temporal shift was acceptable.

Comparison of deconvolution methods

The inclusion of dispersion correction in NSR is a clear advantage compared to the SVD-based methods. Dispersion effects are not expected to be very large in the current application, since QUASAR employs local AIFs, but Petersen et al. have shown that the effects of dispersion on perfusion quantification are not negligible in model-free ASL (31). This agrees with the 4.9% higher perfusion values obtained by NSRcd as compared with NSR. Furthermore, Chappell et al. presented different model-based analysis of QUASAR data, including models with dispersion functions, and demonstrated that the choice of dispersion model substantially affects the perfusion maps (32).

A distinct and very important difference between the methods is that for very noisy voxels (i.e., no apparent bolus passage), NSR generally produces a zero output solution, i.e., 0 ml/100g/min (least penalty on smoothness), whereas SVD tends to return an uncontrollable solution and an unpredictable perfusion value. This observation is especially important in the

context of model-free ASL, since ASL data generally tend to show low SNR and there are, obviously, a number of voxels in which the calculated perfusion values are not reliable. This is also the reason why we removed obviously erroneous voxels from the mean perfusion value in our comparisons.

The current implementation of NSR is indeed very processing intensive, compared to SVD. As an example, one voxel takes approximately 10 ms to compute for oSVD and 2 s for NSR/NSRcd, which results in approximately 4 hours of computation time for a whole brain analysis with NSR (single thread on 2 GHz processor). This is a major drawback which makes NSR algorithms less practical in routine clinical applications.

Spatial variability

Figure 8 shows parametric maps from all ten subjects coregistered into the MNI152 template. In this context, we regarded NSRcd as the proposed method and oSVD as the standard deconvolution method in model-free ASL, so only differences between these two methods were presented. As seen in Figure 8 b-c, the mean estimated perfusion was higher in most areas with NSRcd compared to oSVD. Figure 8 e suggests that the largest differences appeared in areas close to large arteries (high SNR and small delay effects; cf. Fig. 8 i). Potential overestimation in such areas could be explained by residual arterial signal contributions in the measured signal due to imperfect crushing, as suggested by Chappell et al. (32). In such a case, NSRcd would seem to be more susceptible to such errors. Figure 8 f shows that oSVD resulted in higher relative perfusion in WM, watershed areas and posterior regions, which correlated well with areas with higher estimated dispersion effects and long microvascular arrival times (Fig. 8 h-i). This observation might seem somewhat counterintuitive since NSRcd should correct for underestimation due to dispersion effects. However, it may equally well be the lack of dispersion correction (with associated lower absolute CBF estimates) that resulted in higher relative perfusion for oSVD. As a further complexity, areas with long τ_m tend to exhibit lower SNR and are therefore more prone to errors with all deconvolution methods.

More dispersion is expected in distal perfusion territories and it is encouraging that NSR seemed to be able to return a reasonable spatial variation of dispersion effects. Although QUASAR employs local AIFs, the vascular signal must be high for a potential AIF to be accepted. Thus, selected AIFs are expected to be sparse in areas with late arrival times and, similarly, areas with low SNR, which in turn are expected in watershed areas and WM. Although the estimated dispersion effects in GM were smaller than in WM (Fig. 8 h), the quantitative perfusion estimates still suggest that they are not in any way negligible.

Conclusions

In the present work we found that perfusion quantification by model-free ASL is largely dependent on the selected deconvolution method. The NSR deconvolution method was applicable to QUASAR data and produced realistic perfusion-scaled residue functions with little or no oscillations, continuous shape, nonnegative values and, additionally, monotonic decrease when dispersion correction was used. This is encouraging since a more realistic solution should correspond to a perfusion estimate closer to the true perfusion. The implementation resulted in plausible perfusion maps and reasonable absolute GM perfusion values. The perfusion values were significantly higher with our NSR implementation compared to the common SVD methods. Simulations confirmed that the NSR methods generally tend to return more accurate perfusion estimates than the SVD methods.

Acknowledgments

This project was supported by the Swedish Research Council (grant nos. 13514, 2005-6910, 2007-3974 and 2007-6079), the Crafoord foundation, the Lund University Hospital Donation Funds and the Swedish Cancer Society, grant no. 2009/1076.

References

1. Rempp KA, Brix G, Wenz F, Becker CR, Guckel F, Lorenz WJ. Quantification of regional cerebral blood flow and volume with dynamic susceptibility contrast-enhanced MR imaging. Radiology 1994;193:637-41.
2. Østergaard L, Weisskoff RM, Chesler DA, Gyldensted C, Rosen BR. High resolution measurement of cerebral blood flow using intravascular tracer bolus passages. Part I: Mathematical approach and statistical analysis. Magn Reson Med 1996;36:715-25.
3. Detre JA, Leigh JS, Williams DS, Koretsky AP. Perfusion imaging. Magn Reson Med 1992;23:37-45.
4. Williams DS, Detre JA, Leigh JS, Koretsky AP. Magnetic resonance imaging of perfusion using spin inversion of arterial water. Proc Natl Acad Sci U S A 1992;89:212–216.
5. Østergaard L, Sorensen AG, Kwong KK, Weisskoff RM, Gyldensted C, Rosen BR. High resolution measurement of cerebral blood flow using intravascular tracer bolus passages. Part II: Experimental comparison and preliminary results. Magn Reson Med 1996;36:726-36.
6. Wolf RL, Detre JA. Clinical neuroimaging using arterial spin-labeled perfusion magnetic resonance imaging. Neurotherapeutics 2007;4:346-59.
7. Dijkhuizen RM, Nicolay K. Magnetic resonance imaging in experimental models of brain disorders. J Cereb Blood Flow Metab 2003;23:1383-402.
8. Chen W, Song X, Beyea S, D'Arcy R, Zhang Y, Rockwood K. Advances in perfusion magnetic resonance imaging in Alzheimer's disease. Alzheimers Dement 2011;7:185-96.
9. Fernández-Seara MA, Mengual E, Vidorreta M, Aznárez-Sanado M, Loayza FR, Villagra F, Irigoyen J, Pastor MA. Cortical hypoperfusion in Parkinson's disease assessed using arterial spin labeled perfusion MRI. NeuroImage 2012;59:2743-2750.
10. Petersen ET, Lim T, Golay X. Model-free arterial spin labeling quantification approach for perfusion MRI. Magn Reson Med 2006;55:219-32.
11. Buxton RB, Frank LR, Wong EC, Siewert B, Warach S, Edelman RR. A general kinetic model for quantitative perfusion imaging with arterial spin labeling. Magn Reson Med 1998;40:383-96.

12. Wirestam R, Andersson L, Ostergaard L, Bolling M, Aunola JP, Lindgren A, Geijer B, Holtas S, Stahlberg F. Assessment of regional cerebral blood flow by dynamic susceptibility contrast MRI using different deconvolution techniques. Magn Reson Med 2000;43:691-700.

13. Wu O, Østergaard L, Weisskoff RM, Benner T, Rosen BR, Sorensen AG. Tracer arrival timing-insensitive technique for estimating flow in MR perfusion-weighted imaging using singular value decomposition with a block-circulant deconvolution matrix. Magn Reson Med 2003;50:164-174.

14. Murase K, Shinohara M, Yamazaki Y. Accuracy of deconvolution analysis based on singular value decomposition for quantification of cerebral blood flow using dynamic susceptibility contrast-enhanced magnetic resonance imaging. Phys Med Biol 2001;46:3147-59.

15. Calamante F, Gadian DG, Connelly A. Delay and dispersion effects in dynamic susceptibility contrast MRI: Simulations using singular value decomposition. Magn Reson Med 2000;44:466-73.

16. Calamante F, Gadian DG, Connelly A. Quantification of bolus-tracking MRI: Improved characterization of the tissue residue function using Tikhonov regularization. Magn Reson Med 2003;50:1237-1247.

17. Andersen IK, Szymkowiak A, Rasmussen CE, Hanson LG, Marstrand JR, Larsson HBW, Hansen LK. Perfusion quantification using Gaussian process deconvolution. Magn Reson Med 2002;48:351-361.

18. Willats L, Connelly A, Calamante F. Improved deconvolution of perfusion MRI data in the presence of bolus delay and dispersion. Magn Reson Med 2006;56:146-156.

19. Zanderigo F, Bertoldo A, Pillonetto G, Cobelli Ast C. Nonlinear stochastic regularization to characterize tissue residue function in bolus-tracking MRI: Assessment and comparison with SVD, block-circulant SVD, and Tikhonov. IEEE Trans Biomed Eng 2009;56:1287-97.

20. Petersen ET, Mouridsen K, Golay X. The QUASAR reproducibility study, Part II: Results from a multi-center arterial spin labeling test-retest study. Neuroimage 2010;49:104-13.

21. Petersen ET. Brain perfusion imaging: Quantification of cerebral blood flow using ASL techniques. Aarhus: Aarhus University; 2009.

22. Zanderigo F. Assessment of cerebral hemodynamics by deconvolution with dynamic susceptibility contrast - magnetic resonance imaging. Padua: University of Padua; 2006.

23. Peruzzo D, Zanderigo F, Bertoldo A, Pillonetto G, Cosottini M, Cobelli C. Assessment of clinical data of nonlinear stochastic deconvolution versus block-circulant singular value decomposition for quantitative dynamic susceptibility contrast magnetic resonance imaging. Magn Reson Imaging 2011;29:927-36.

24. Ahlgren A, Wirestam R, Ståhlberg F, Knutsson L. Using fractional segmentation for estimation of the equilibrium magnetization of arterial blood in model-free arterial spin labeling. In Proceedings of the 28th Annual Scientific Meeting of ESMRMB, Leipzig, Germany, 2011, 554.

25. Shin W, Geng X, Gu H, Zhan W, Zou Q, Yang Y. Automated brain tissue segmentation based on fractional signal mapping from inversion recovery Look-Locker acquisition. Neuroimage 2010;52:1347-54.

26. Ozyurt O, Dincer A, Ozturk C. A modified version of Hrabe-Lewis model to account dispersion of labeled bolus in arterial spin labeling. In Proceedings of the ISMRM-ESMRMB Joint Annual Meeting, Stockholm, Sweden, 2010, 4065.

27. Canny J. A computational approach to edge detection. IEEE Trans Pattern Anal Mach Intell 1986;8:679-98.

28. Lu H, Clingman C, Golay X, van Zijl PCM. Determining the longitudinal relaxation time (T1) of blood at 3.0 Tesla. Magn Reson Med 2004;52:679-682.

29. Friston KJ, Ashburner J, Frith CD, Poline JB, Heather JD, Frackowiak RSJ. Spatial registration and normalization of images. Hum Brain Mapp 1995;3:165-189.

30. Leenders KL, Perani D, Lammertsma AA, Heather JD, Buckingham P, Healy MJ, Gibbs JM, Wise RJ, Hatazawa J, Herold S and others. Cerebral blood flow, blood volume and oxygen utilization. Normal values and effect of age. Brain 1990;113 (Pt 1):27-47.

31. Petersen ET, Golay X. The effect of bolus length and dispersion on arterial spin labeling flow quantification In Proceedings of the ISMRM-ESMRMB Joint Annual Meeting, Stockholm, Sweden, 2010, 514.

32. Chappell MA, Woolrich MW, Petersen ET, Golay X, Payne SJ. Comparing model-based and model-free analysis methods for QUASAR arterial spin labeling perfusion quantification. Magn Reson Med 2012;DOI:10.1002/mrm.24372.

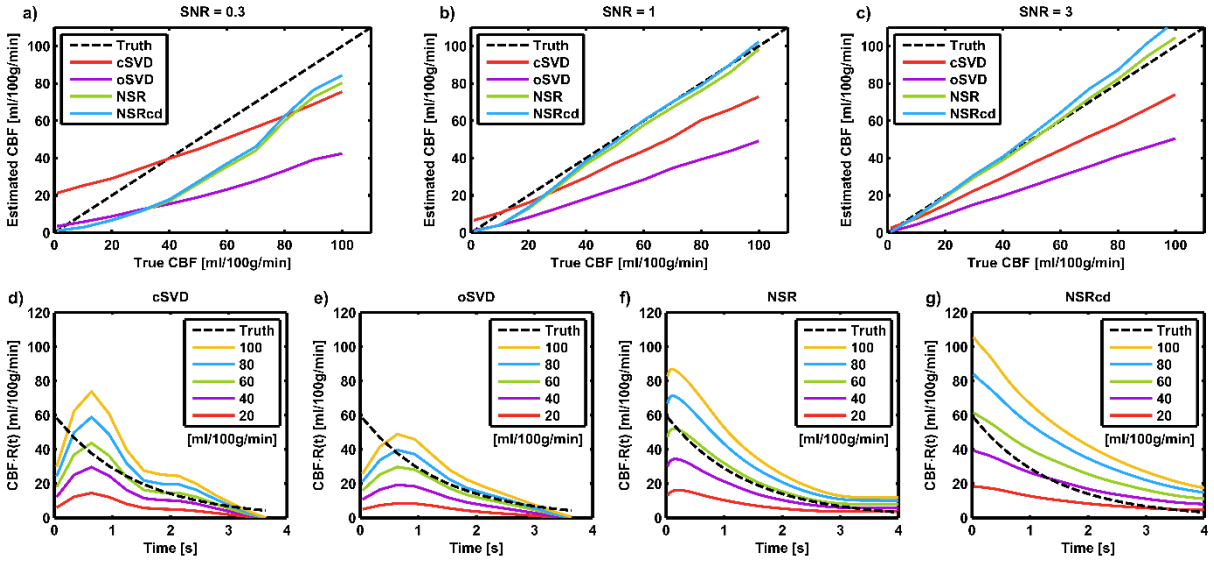

Figure 1. Simulations of perfusion and residue function estimation using the different deconvolution methods under investigation. Top row displays estimated perfusion as a function of true perfusion, using SNR levels of 0.3, 1 and 3 (a,b and c, respectively). The botttom row (d-i) shows mean residue functions (n=1000) for a selection of perfusion values between 20 and 100 ml/100g/min and SNR=1, using cSVD, oSVD, NSR and NSRcd, respectively. The black dashed line represents the true residue function for 60 ml/100g/min.

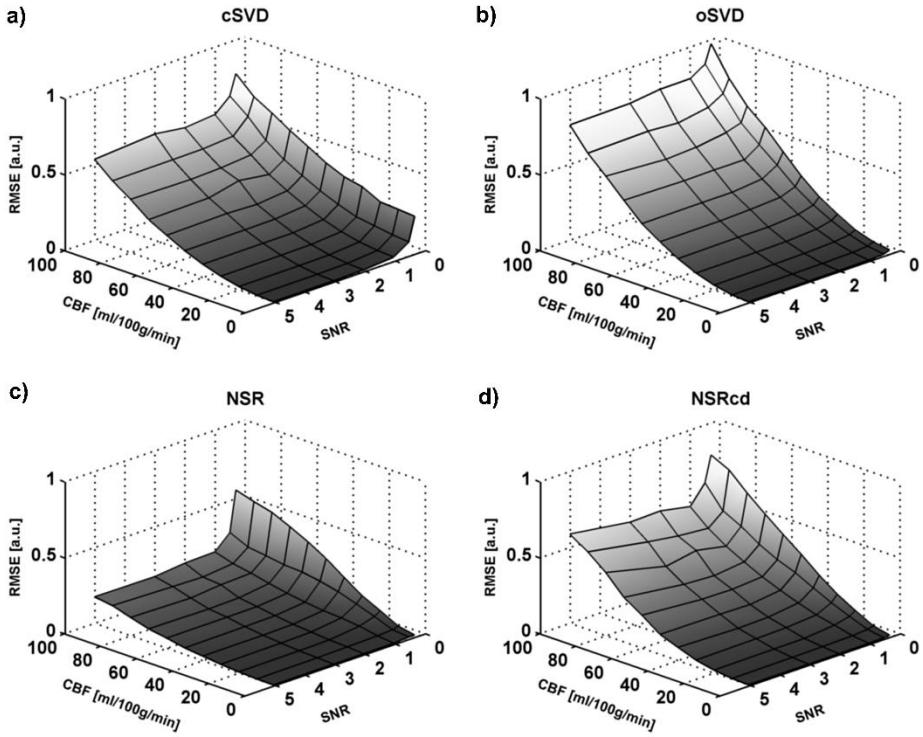

Figure 2. Root-mean-square error of the estimted residue functions from the simulations (in arbitrary units) as a function of CBF and SNR for: (a) cSVD, (b) oSVD, (c) NSR and (d) NSRcd.

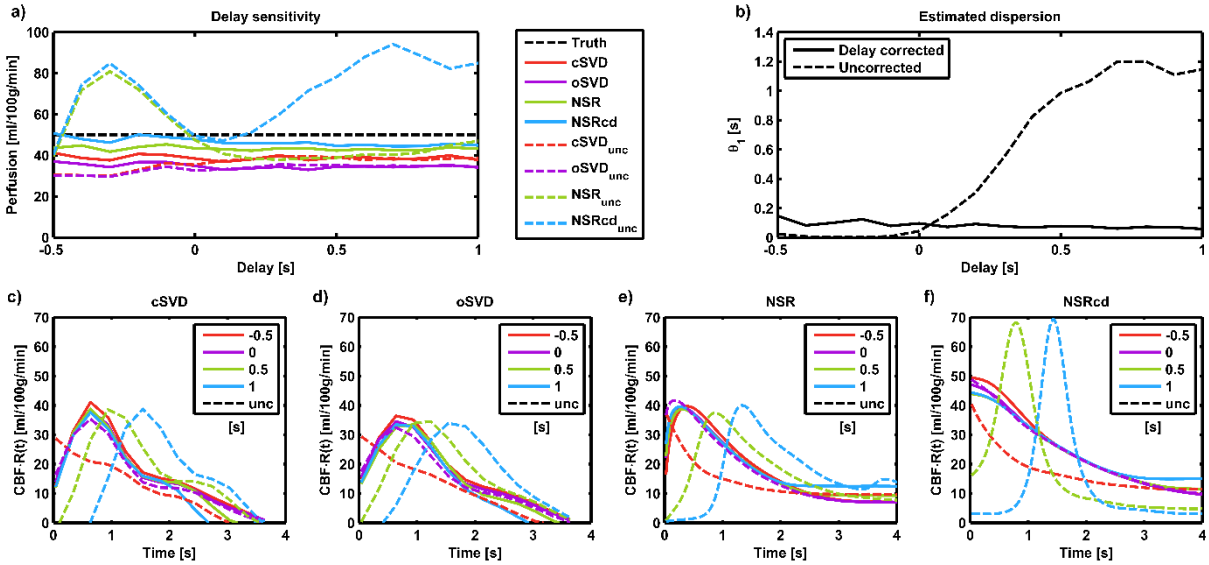

Figure 3. Simulations of the delay sensitivity of the deconvolution methods with (solid lines) and without (dashed lines) delay correction: (a) Estimated perfusion as a function of the delay (black dashed line is the true perfusion of 50 ml/100g/min). (b) Dispersion (θ_1) estimated by NSR as a function of delay. (c-f) Mean residue functions (n=1000) for a selection of delays between -0.5 and 1 s, using cSVD, oSVD, NSR and NSRcd, respectively (unc=uncorrected).

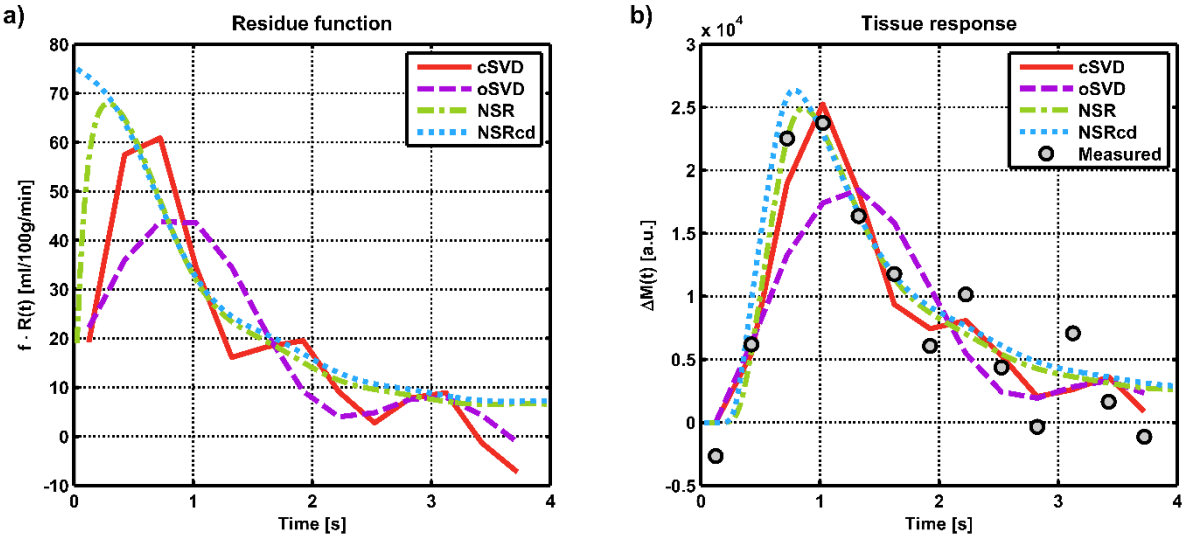

Figure 4. Example of deconvolution results from a representative grey matter voxel in one subject. a) Residue functions as obtained by cSVD (red solid), oSVD (blue dashed), NSR (green dash-dotted) and NSRcd (pink dotted). b) Measured tissue response (circles), and the corresponding reconvolved tissue responses.

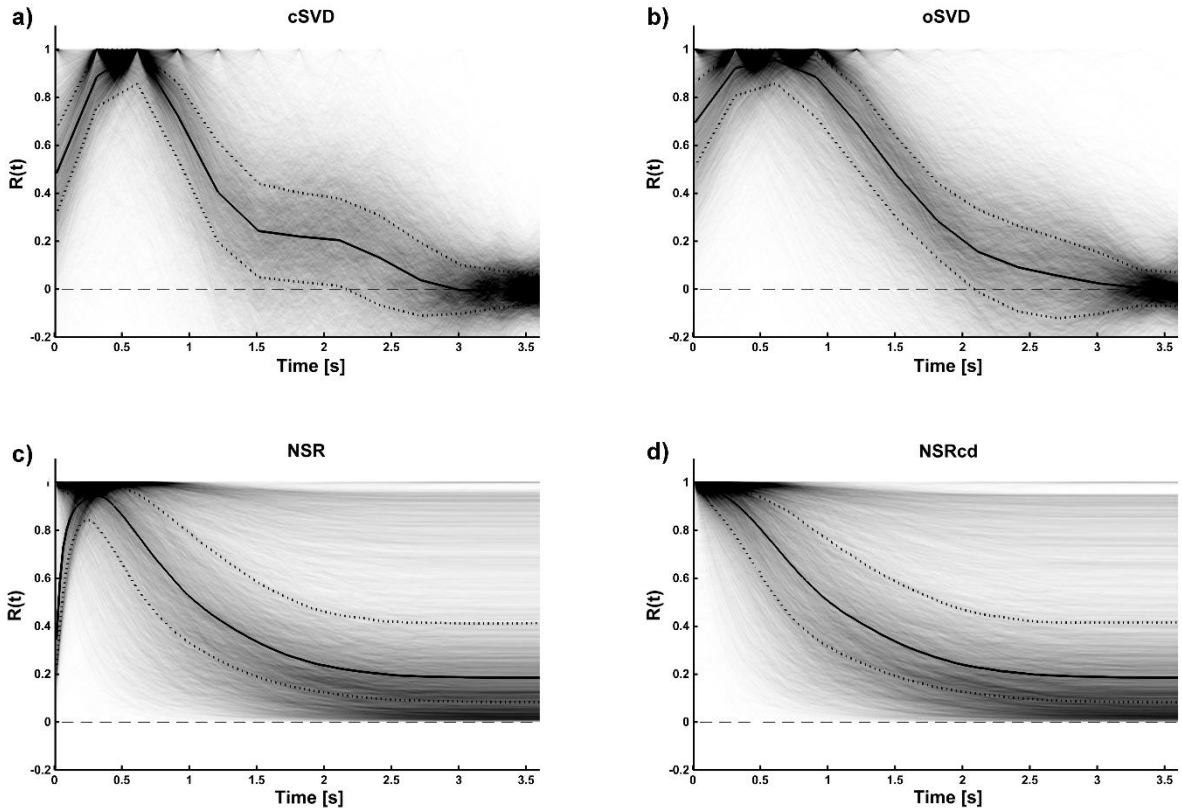

Figure 5. Density plot of normalized residue functions from all grey matter voxels in all subjects, for cSVD (a), oSVD (b), NSR (c) and NSRcd (d). The solid line is the median, and dotted lines are the 25th and 75th percentiles.

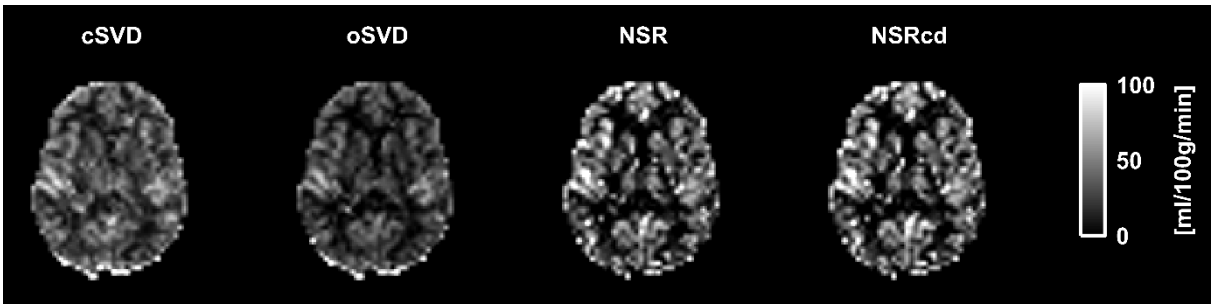

Figure 6. Parametric CBF maps obtained by the different deconvolution methods. Example from one slice in subject 1.

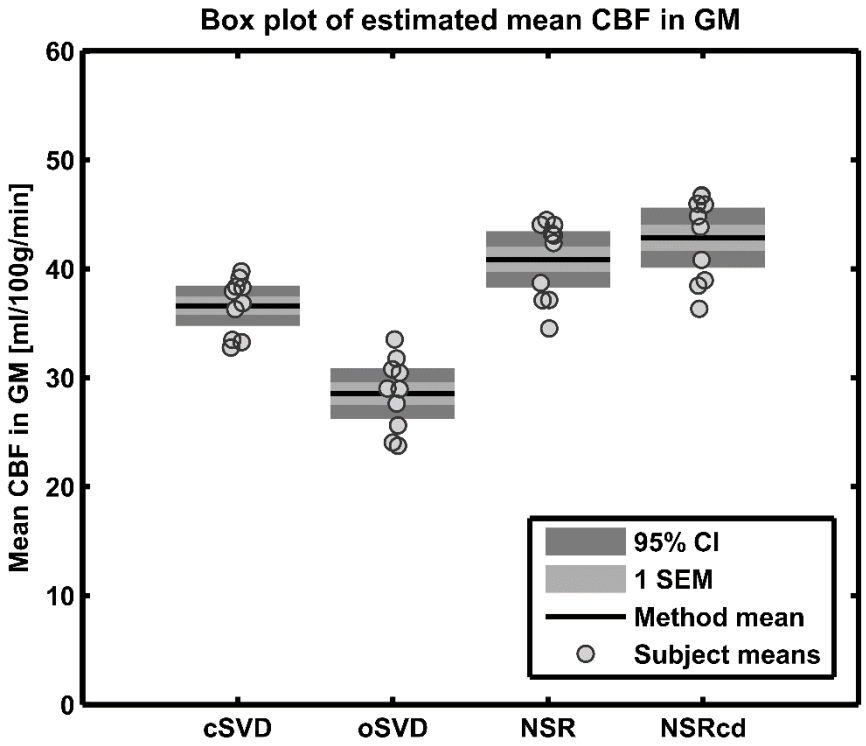

Figure 7. Box plot of subject CBF_{GM} for the different methods. Black lines are the means of the subject CBF_{GM} (method means), light grey areas represent one standard error of mean (SEM), and grey areas is the 95% confidence intervals (CI). All methods except NSR and NSRcd showed significantly different means ($p<0.05$).

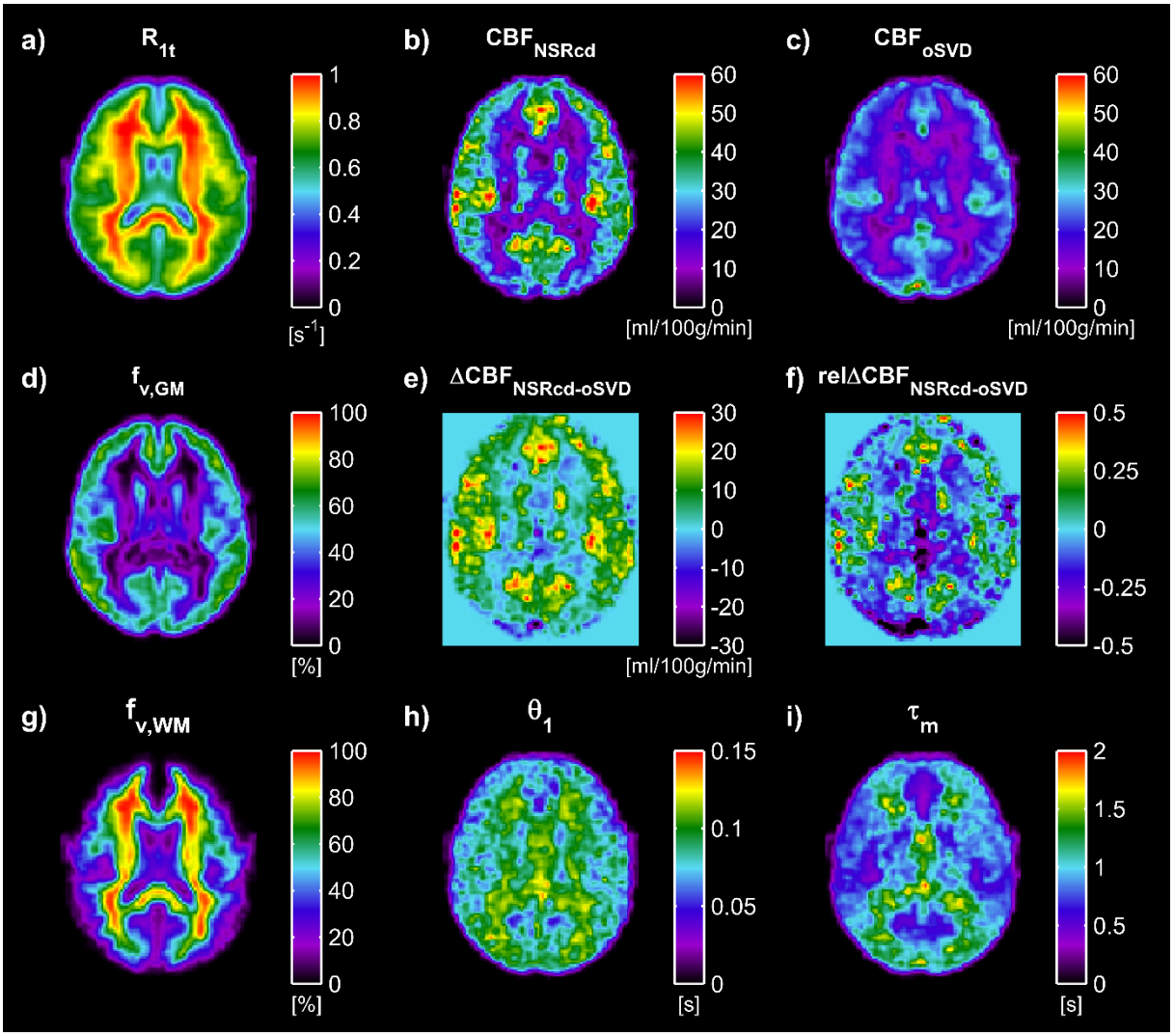

Figure 8. Spatial variability analysis with mean parametric maps based on all ten subjects coregistered into MNI space: (a) Longitudinal relaxation rate ($R_{1t} = 1/T_{1t}$). (b) Perfusion estimates obtained by NSRcd. (c) Perfusion estimates obtained by oSVD. (d) Fractional volume of GM. (e) Absolute difference in estimated perfusion between NSRcd and oSVD. (f) Relative difference in estimated perfusion between NSRcd and oSVD (normalized subject and method-wise by CBF_{GM}). (g) Fractional volume of WM. (h) Dispersion estimated by NSR. (i) Time point of the rising edge of the crushed tissue signal (microvascular arrival time).

Table 1. Mean GM perfusion values in ml/100g/min for all subjects and deconvolution methods, with one standard deviation in parenthesis.

Subject	**cSVD**	**oSVD**	**NSR**	**NSRcd**
1	37.9 (18)	30.5 (11)	44.0 (23)	46.0 (24)
2	33.3 (20)	24.0 (14)	37.1 (29)	38.9 (30)
3	36.3 (23)	27.6 (17)	34.5 (26)	36.3 (27)
4	38.4 (19)	31.8 (13)	42.4 (25)	43.8 (26)
5	33.5 (17)	25.6 (14)	38.7 (24)	40.8 (26)
6	36.8 (18)	29.0 (13)	43.1 (23)	46.7 (26)
7	39.2 (19)	30.8 (13)	44.5 (28)	46.7 (29)
8	39.8 (21)	33.5 (15)	44.1 (26)	45.9 (27)
9	38.3 (19)	29.0 (12)	43.2 (27)	44.8 (28)
10	32.8 (19)	23.8 (11)	37.1 (26)	38.4 (26)
Mean	**36.6 (2.6)**	**28.6 (3.3)**	**40.9 (3.6)**	**42.9 (3.9)**